remote sensing

MDPI

Article

A Fully Automatic Instantaneous Fire Hotspot Detection Processor Based on AVHRR Imagery—A TIMELINE Thematic Processor

Simon Plank *, Eva-Maria Fuchs and Corinne Frey

German Aerospace Center (DLR), German Remote Sensing Data Center (DFD), Muenchener Str. 20, 82234 Oberpfaffenhofen, Germany; Eva-Maria.Fuchs@dlr.de (E.-M.F.); Corinne.Frey@dlr.de (C.F.)

* Correspondence: simon.plank@dlr.de; Tel.: +49-8153-28-3460

Academic Editors: Ruiliang Pu, Ioannis Gitas and Prasad S. Thenkabail

Received: 26 September 2016; Accepted: 28 December 2016; Published: 2 January 2017

Abstract: The German Aerospace Center's (DLR) TIMELINE project aims to develop an operational processing and data management environment to process 30 years of National Oceanic and Atmospheric Administration (NOAA)—Advanced Very High Resolution Radiometer (AVHRR) raw data into L1b, L2 and L3 products. This article presents the current status of the fully automated L2 active fire hotspot detection processor, which is based on single-temporal datasets in orbit geometry. Three different probability levels of fire detection are provided. The results of the hotspot processor were tested with simulated fire data. Moreover, the processing results of real AVHRR imagery were validated with five different datasets: MODIS hotspots, visually confirmed MODIS hotspots, fire-news data from the European Forest Fire Information System (EFFIS), burnt area mapping of the Copernicus Emergency Management Service (EMS) and data of the Piedmont fire database.

Keywords: hotspot detection; AVHRR; automatic processor; TIMELINE

1. Introduction

Forest fires are a natural component which regulate the evolution, productivity and biodiversity of natural plant communities and ecosystems since millennia [1,2]. Many vegetation communities have developed as a response to fires, which leads to a higher abundance of species-richness in burned ecosystems [3]. However, since humans started to change flora and fauna, and set artificial fires, wildfires have become one of the most devastating natural hazards worldwide. They destroy environment and property, impact air quality, contribute to global warming and even threaten lives [4–14]. In many cases, vegetation fires occur in remote areas which complicate their detection, mapping and extinguishing. Hence, medium resolution satellites are currently the only solution to frequently map active fires and quantify fire emissions at regional to global scales. However, not only ongoing observation is relevant: for a detailed understanding of fire ecosystems, the terrestrial-atmospheric interactions and the impact of wildfires to global change, it is of utmost importance to map historical fire events accurately, reliably, objectively and consistently [15]. Thus, the Advanced Very High Resolution Radiometer (AVHRR) on board the National Oceanic and Atmospheric Administration's (NOAA) polar orbiting satellites represents a unique data source, as satellite images are available since 1978/1980 and their spatial resolution and spectral capabilities are suitable to detect forest fires. The goal of the TIMELINE project lies in acquiring a consistent database of hotspots in Europe for more than 30 years. These data could be important for various research fields, e.g., climate change analysis, atmospheric chemistry, forest management and ecosystem functioning, survey and penalization and wildlife management.

1.1. Issues of Active Fire Detection

As AVHRR was mainly designed for weather surveillance and sea surface temperature management, it contains some weaknesses for forest fire detection: A differentiation between fires and normal earth temperatures is not an easy task, as (during daytime) not only fires, but also highly reflective soils or sun glint easily saturate channel 3 [16,17]. The wide scan angle (±55°) causes degradation in spatial resolution up to 2.5 km × 7 km to the scene margins. Channel degradation over time causes decreases in measurement precision [18], and orbital drift causes variations in AVHRR observations with respect to solar position [19]. Moreover, earth observation in general has problems concerning obscuration by clouds, contamination of temperatures by clouds [20], and absorption and reflection of radiant energy from fires by overstory canopy. As fires typically manifest a strong diurnal rhythm, fire measurements from a sensor platform with a fixed hour of observation may have strong biases.

Being aware of these weaknesses, AVHRR shows also several advantages for active fire detection: AVHRR's channel 3 and channel 4 are suitable to detected fires (please find more information regarding this topic in Section 1.2 and [21]). The spatial degradation to the scene margins appears to have scarce effects on its ability to detect hotspots [22]. Problems regarding channel degradation and orbital drift could be minimized within the TIMELINE project [23–25]. Moreover, as the spatial coverage of whole Europe within frequent time intervals should be mapped, AVHRR exhibits an appropriate relation between coverage and spatial resolution. Furthermore, AVHRR sensors have been in orbit since 1978/1980, which provide the longest and most consistent time-series available.

1.2. Physics of Active Fire Detection

Radiation of forest fires varies from 500 K for smoldering fires to about 1200 K for flaming fires [26]. Looking at Wien's displacement law shows that the radiation peak from objects emitting at these temperatures is around 2–6 µm, which is partly covered by AVHRR's channel 3. In the middle infrared, fires radiate intensely (to about 1500 times) against a low-energy background. Thus, fires occupying just a small part of a pixel can be detected, as well as big and cool fires. As AVHRR's channel 4 (cf. Table 1) is about 45 times less sensitive to high temperatures than channel 3, and is not affected by solar reflection, differences in brightness temperatures between channel 3 and channel 4 can be used to avoid false alarms due to highly reflective soils, naturally hot surfaces (e.g., deserts) and sun glint [26]. Thus, hotspot detection with AVHRR means, that only intensely radiating fires (which can cover only a small part of an AVHRR pixel), or bigger and cooler fires covering larger areas can be detected.

1.3. Methods for Active Fire Detection

Considering the long time availability of AVHRR, forest fires in various biomes and landscapes, e.g., tropical forests [10,27–36], boreal areas [21,37–44], straw burning [45–48], savannahs [16,26,49–51] and the Mediterranean [52–54], have been developed.

First approaches relied on the detection capability of channel 3 only [32,52,55]. Later, multi-threshold algorithms have been developed [21,26,30,32,38,40,41,56–58]. These methods are based on the definition of empirical thresholds for decision tests. Afterwards, more sophisticated contextual algorithms have been applied [33,34,42,43,54,59–64], which exploit the strong temperature contrast among hot fire pixels and their cold background by calculating spatial statistics (e.g., average value and standard deviation) within variable sized windows around candidate fire pixels. In addition, various other methods relying on statistical approaches applied to historical satellite records have been developed [65–68]. Not only daytime overpasses, but also nighttime images have been used for forest fire detection [50,69]. There, solar reflection is negligible and wildfires can be detected by applying fixed thresholds to channels 3 and 4. Nevertheless, the problems of obscuration due to clouds and misclassification of clouds are still present.

An extensive round robin approach which tested and validated different methods and thresholds has shown that the contextual algorithm performs best for hotspot detection with AVHRR [70]. Therefore, a further enhancement of the contextual algorithm of Giglio et al. [61] is used for final implementation (cf. Section 3).

1.4. The TIMELINE Project

This article presents a fully automated contextual level 2 (L2) hotspot detection algorithm for analysis of AVHRR imagery. L2 means that only single datasets in the satellite's orbit geometry are processed. The developed hotspot detection algorithm is part of the German Aerospace Center's (DLR) TIMELINE project, which aims to develop an operational processing and data management environment to reprocess 30 years of NOAA-AVHRR raw data into L1b, L2 and L3 products on the basis of 1.1 km High Resolution Picture Transmission (HRPT) and Local Area Coverage (LAC) data of the European continent and offer them online to a wider community using a free and open data policy. Therefore, an enhanced pre-processing by taking geometric distortions due to rotation and satellite clock errors, varying spectral responses of different AVHRR sensors, calibration drift, orbit drift, sensor degradation and atmospheric correction into account is performed [23–25]. Consistency of calibrated reflectance and thermal information is highly required for time series analysis as planned within TIMELINE [71,72]. Furthermore, enhanced cloud masks, water masks, snow masks and land use/land cover products are developed based on accurate and continuous L1b products. As the project is still ongoing, the preprocessing and derivation of L2 products is not finished yet. Thus, the hotspot product is steadily in progress, and, within this paper, a detailed description of current state of the L2 hotspot product (Section 3) is presented.

2. Materials and Methods

2.1. Study Sites and Data

Europe offers a high diversity of ecosystems with tundra, alpine tundra, taiga, montane forest, temperate broadleaf forest, Mediterranean forest and temperate steppe. The main natural vegetation cover is mixed forest, such as mixed forest with broadleaf and coniferous trees in temperate Europe, beech and oak in central and western Europe, the taiga (mixed spruce-pine-birch forest) of Scandinavia and Russia, mixed rainforests of the Caucasus and the cork oak, holm oak, kermes oak and pine forests, scrub forest, olive trees, conifers and cypresses in the Mediterranean. The high biodiversity is a result of diverse climates. With the exception of the Far East coast, precipitation decreases to the north and east. Thus, whilst Western Europe has an oceanic climate, Eastern Europe has a drier, continental climate. Parts of the central European plains have a hybrid oceanic/continental climate. The Mediterranean Basin is influenced by a warm maritime climate, with wet and mild winters and dry and hot summers. These conditions make the Mediterranean prone to forest fires, primarily in the late summer months, when the vegetation suffers from water stress.

The test sites where the developed hotspot detection processor was validated are located in different European regions: Portugal, Greece, Sicily, Piedmont and Sweden (Figure 1).

Pre-processed (top of atmosphere reflectances and brightness temperatures) L1b AVHRR data is used as input for the hotspot detection processor [23–25]. The first AVHRR sensor was launched with TIROS-N in 1978. Since then, the AVHRR sensor has been launched onboard a long series of satellites (NOAA-1 to NOAA-19, Met-OP-A). Three different generations of AVHRR sensors have been in orbit. Table 1 shows their spectral descriptions.

Channels 3B and 4 are used within the proposed fire detection procedure. Channels 1, 2 and 5 are used for the generation of the exclusion masks (cf. Section 3). AVHRR imagery containing only the channel 3A and not data of channel 3B is not suitable for the hotspot detection.

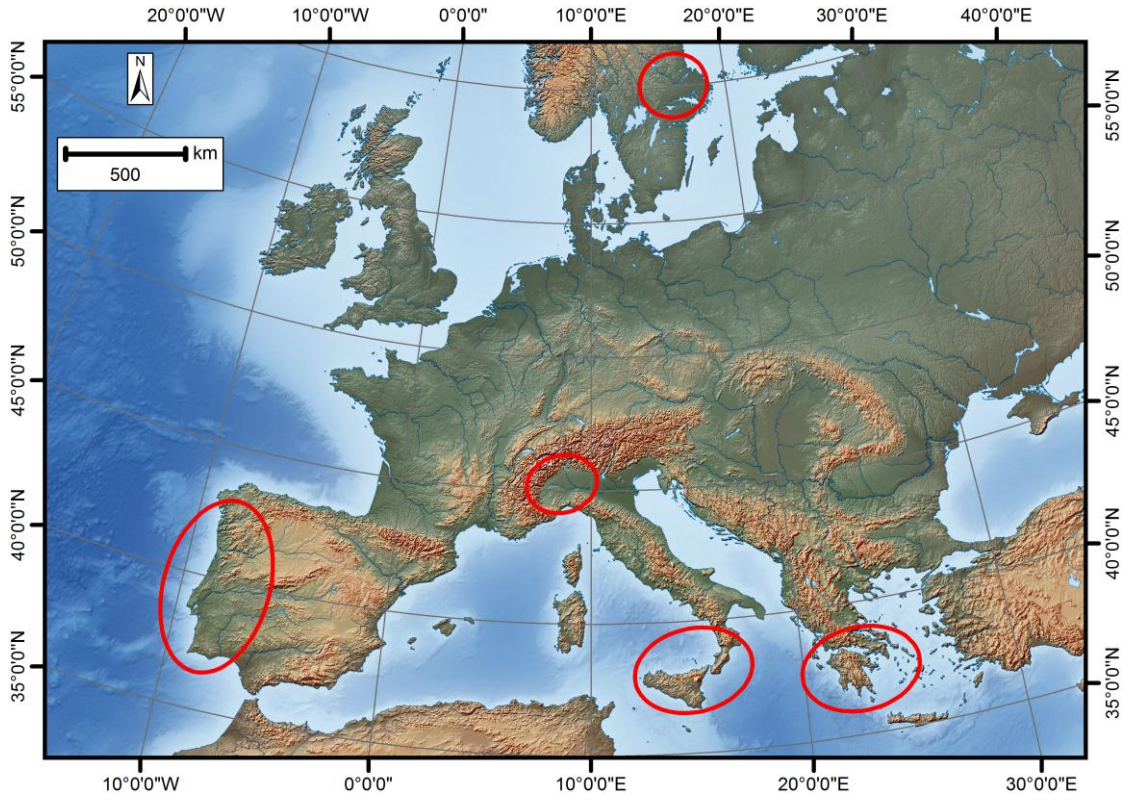

Figure 1. Overview map of the test sites Portugal, Sicily, Piedmont, Greece and Sweden (red circles).

Table 1. Spectral descriptions of the AVHRR sensors.

Channel	AVHRR-1: NOAA-6, -8, -10	AVHRR-2: NOAA-7, -9, -11, -12, -14	AVHRR-3: NOAA-15, -16, -17, -18, -19
1	0.58–0.68	0.58–0.68	0.58–0.68
2	0.725–1.1	0.725–1.1	0.725–1.1
3A	-	-	1.58–1.64
3B	3.55–3.93	3.55–3.93	3.55–3.93
4	10.5–11.5	10.3–11.3	10.3–11.3
5		11.5–12.5	11.5–12.5

2.2. Method

Based on the algorithm proposed by Giglio et al. [61] a further enhanced, fully automated contextual algorithm has been implemented in the Interactive Data Language (IDL). This algorithm intends to map as many active fires as possible, but, as already stated in Sections 1.1 and 1.2, mainly very hot fires (which can cover only a small part of an AVHRR pixel), or bigger and cooler fires covering larger areas.

2.2.1. Description of Exclusion Masks

To reduce the possibility of false (over) classification, several land cover classes and disturbing objects are excluded prior to the detection of the fire hotspots. As fires could not occur in areas covered by water—with the exception of burning oil spills which are not the focus of our study—all water areas are excluded. The water areas are derived from a land use and land cover (LULC) classification [73]. To guarantee that non-permanent water areas or water areas missing in the LULC classification are also excluded, water areas are also derived directly from the satellite imagery (Equation (1)) [74].

$$water = \frac{{\mu_{1,2}}^2}{\sigma_{1,2}} \langle \vartheta_W \wedge ch_1 \rangle ch_2 \quad (1)$$

with ch_i = channel 1 or 2 of the AVHRR imagery, $\mu_{1,2}$ = mean of ch_1 and ch_2, $\sigma_{1,2}$ = standard deviation of ch_1 and ch_2, and ϑ_W = threshold for water areas.

As a sensor using the visible to the thermal infrared part of the electromagnetic spectrum, AVHRR is not able to penetrate clouds. Therefore, areas covered by clouds are excluded (Equation (2)) [74]. This is especially necessary, as the contextual hotspot detection processor (described in Section 2.2.2) searches for strong contrast between neighboring pixels. Borders of clouds and water areas are characterized by such a strong contrast and are therefore a source of false classifications.

$$clouds = \left(W_{ch_3} W_{\delta_{ch}} \mu_{1,2}\right) > \vartheta_C \quad (2)$$

with ϑ_C threshold for cloud areas,

$$W_{ch_3} = \exp\left(\frac{310 - T_3}{20}\right) \quad (3)$$

and

$$W_{\delta_{ch}} = \exp\left(\frac{\left(T_3 - \frac{T_4 + T_5}{2}\right) - 14}{14}\right) \quad (4)$$

with brightness temperature T_i of channel i.

As the hotspot detection processor could falsely interpret sun glint as high temperature objects, the areas of possible sun glint occurrence are pre-calculated according to Giglio et al. [75] and are excluded from the further processing. Therefore, in the case of a daytime acquisition, the angle between vectors pointing in the surface-to-satellite and specular reflection directions, θ_g, is calculated (Equation (5)).

$$\cos\left(\theta_g\right) = \cos\theta_{sat} \cos\theta_{sun} - \sin\theta_{sat} \sin\theta_{sun} \cos\phi \quad (5)$$

with θ_{sat}, θ_{sun} and ϕ representing the satellite viewing zenith angle, the solar zenith angle and the relative azimuth angle, respectively. The relative azimuth angle ϕ depends on the sun azimuth angle ϕ_{sun} and the satellite azimuth angle ϕ_{sat} (Equation (6)).

$$\phi = |\phi_{sun} - \phi_{sat}| \quad (6)$$

AVHRR pixels are excluded for sun glint if following conditions are true (Equations (7) and (8), with all angles measured in degrees):

$$\theta_g < 5^\circ \quad (7)$$

$$\theta_g < 15^\circ \wedge ch_2 > 0.2, \quad (8)$$

Urban areas and especially desert areas could show temperature values (up to 340 K) which are over the saturation temperature of the AVHRR sensor (322 to 331 K). Consequently, these LULC classes have to be excluded prior the execution of the core hotspot detection processor. As a first step, the LULC layer described above is used to remove the class bare land (including desert areas) as well as urban area. Furthermore, as the spatial resolution of the LULC is with 1 km not high enough to cover also smaller towns, the global urban footprint (GUF) is used as an additional source. The GUF is derived from the local speckle statistics of TanDEM-X SAR imagery [76]. The original spatial resolution (0.4 arc seconds, which is equal to ca. 12 m) of the GUF was resampled to 1 km. However, to preserve the higher spatial resolution information for each 1 km pixel the percentage of urban area was calculated. All areas with an urban coverage of >20% are excluded.

Wild fires—which are the focus of our processor—require a certain volume of vegetation as fuel. To further reduce false classifications due to bare areas which are not covered by the rough resolution LULC classification, the so-called fraction of vegetation (*FVC*) was calculated (Equation (9)) [77]. All areas with a $FVC < 0.1$ are excluded.

$$FVC = \left(\frac{NDVI - \min_{NDVI}}{\max_{NDVI} - \min_{NDVI}} \right)^2 \quad (9)$$

with $\min_{NDVI}$ and $\max_{NDVI}$ representing the minimum and maximum value of the NDVI within the analyzed AVHRR scene. The Normalized Difference Vegetation Index (NDVI) is a proxy for the site's vegetation density and greenness [78–81]. The NDVI uses the difference of the vegetation signature between the RED (ch_1) and Near Infrared (ch_2) channel (Equation (10)).

$$NDVI = \frac{ch_2 - ch_1}{ch_2 + ch_1} \quad (10)$$

As described in Section 1, the AVHRR sensor is characterized by a wide scan angle ($\pm 55^\circ$). This leads to a rough resolution up to 2.5 km $\times$ 7 km at large scan angles. Consequently, fires at very large scan angles are often not detected [82]. To reduce the missing fire-rate, all areas acquired at a scan angle larger than 40° are excluded from the analysis, i.e., the analysis area is restricted to the area covered by a scan angle smaller than 40°. In the aforementioned fully automated series processor which will be applied within the TIMELINE project, these excluded areas will be covered by neighboring AVHRR scenes. Thus, finally for the entire TIMELINE study area a hotspot detection will be performed on a daily basis.

2.2.2. Core Hotspot Processor

The described hotspot processor is a further development of the one proposed by Giglio et al. [61]. The first step of the core hotspot processor is the selection of possible fires, i.e., hotspot candidates. The proposed processor differs between day-time and night-time acquisitions and performs three different runs with different thresholds, resulting in three different fire probability levels (Table 2, with $T_{3,4}$ being the difference of the brightness temperatures T_3 and T_4).

Table 2. Thresholds for selection of the fire candidates.

Probability Level	T_3 Day-Time (K)	$T_{3,4}$ Day-Time (K)	T_3 Night-Time (K)	$T_{3,4}$ Night-Time (K)
low	310	6	308	4
medium	311	6	309	4
high	312	6	310	4

Valid background pixels are those not excluded as described in Section 3.1, i.e., pixels not covered by water, clouds, bare land or urban area and not affected by sun glint or acquired at too large scan angles. In addition, potential background fire pixels, defined as $T_3 > 318$ K and $T_{3,4} > 12$ K, are excluded from the valid background pixels. The eight direct neighbors of the fire candidates are excluded from the valid background pixels as well.

Next, within a contextual approach around each fire candidate a window of 5 $\times$ 5 pixels, which is increased up to 21 $\times$ 21 pixels, until at least 25% of the background pixels in the window are valid, and the number of valid background pixels is at least six. If an insufficient number of valid background pixels is identified, the fire candidate pixel is classified as unknown, otherwise the following statistics are computed (Table 3).

Table 3. Statistics calculated.

Symbol	Description	Day/Night
$T_{3,4\,B}$	Mean of T_3–T_4	Day & Night
$\delta_{3,4\,B}$	Mean absolute deviation of T_3–T_4	Day & Night
$T_{4\,B}$	Mean of T_3–T_4	Day only
$\delta_{4\,B}$	Mean absolute deviation of T_4	Day only

The mean absolute deviation δ (Equation (11)) is a more robust estimator compared to the standard deviation. δ possess greater statistical efficiency for contaminated normal and some non-normal distributions [56].

$$\delta = \frac{\sum_{i=1}^{N} |x_i - \mu|}{N} \tag{11}$$

for N observations x_i ($i = 1, \ldots, N$) and mean μ.

A fire candidate pixel is classified as a fire if following requirements are fulfilled, otherwise it is classified as non-fire. Equation (12) describes the test for a daytime scene and Equation (13) the test for a nighttime acquisition.

$$T_{3,4} > T_{3,4\,B} + \Delta T \wedge T_4 > T_{4\,B} + \delta_{4\,B} - 3\,\mathrm{K}, \tag{12}$$

$$T_{3,4} > T_{3,4\,B} + \Delta T \tag{13}$$

The resulting fire pixels are assigned to the quality levels low, medium and high according to the condition described in Table 4.

Table 4. Quality of the fire pixels.

Quality	Condition
low	water, clouds, bare land, urban area in 3 × 3 neighborhood to fire pixel
medium	water, clouds, bare land, urban area in 5 × 5 neighborhood to fire pixel
high	water, clouds, bare land, urban area > 5 × 5 neighborhood to fire pixel

3. Results

3.1. Simulated Dataset

As a first step of validation, the proposed hotspot processor was tested based on a simulated dataset of fires under simplified conditions. The model consists of a 50 × 50 pixel testing area with each pixel characterized by a size of 1 km^2, which is equal to the spatial resolution of AVHRR at nadir conditions. The test area is divided into four sectors, each including a simulated fire in its center. The size of these fires range from 10 m^2, 100 m^2, or 1000 m^2 up to 10,000 m^2. Altogether, 60 different conditions were simulated. The following parameters were applied to all four fires: the temperature of the fire itself was varied among 600 K, 800 K and 1000 K; and the background temperature within the fire pixel (remaining area of the fire pixel not covered by the fire) and the surrounding pixels was varied among 240 K, 255 K, 270 K, 285 K and 300 K. All aforementioned temperatures represent the values of T_3. For this simulation T_4 was set T_3—7 K, making $T_{3,4}$ large enough for fire detection.

The simulated fire surface temperatures were transformed to brightness temperature values assuming a fire emissivity of 0.95 (see [61]). The brightness temperature of the entire fire pixel was derived by computing the brightness temperatures of the fire itself and the fire pixel background (temperature of the remaining area of the fire pixel not covered by the fire) to radiance. Then, the average radiance of the fire pixel was computed as a function of the percentage area of the fire within the fire pixel. Next, the resulting average radiance of the fire pixel was computed back to the brightness

temperature of the fire pixel. The transformation from brightness temperature to radiance and back to brightness temperature was done by means of the Planck's equation.

For each of these different conditions it was tested whether the proposed algorithm is able to detect the simulated fires. The first row of Figure 2 shows the positions of the simulated fires and their sizes. The second to forth row show the results of the fire detection for 600 K, 800 K and 1000 K surface temperature of the fire at different temperatures for the remaining area of the fire pixel not covered by the fire (columns). Figure 2 clearly shows that at a fire temperature of 600 K only big fires of an area of 10,000 m^2 or larger can be detected by the proposed algorithm. Only when the temperature of the remaining area of the fire pixel not covered by the fire is warmer, i.e., ~300 K, smaller fires at a temperature of 600 K can also be detected. The results for the 800 K and 1000 K hot fires are similar, except for the test case with a background temperature of 300 K. In this case, even for fires covering an area of 100 m^2 the resulting average temperature of the fire pixel is hot enough to be detected by the hotspot detection algorithm.

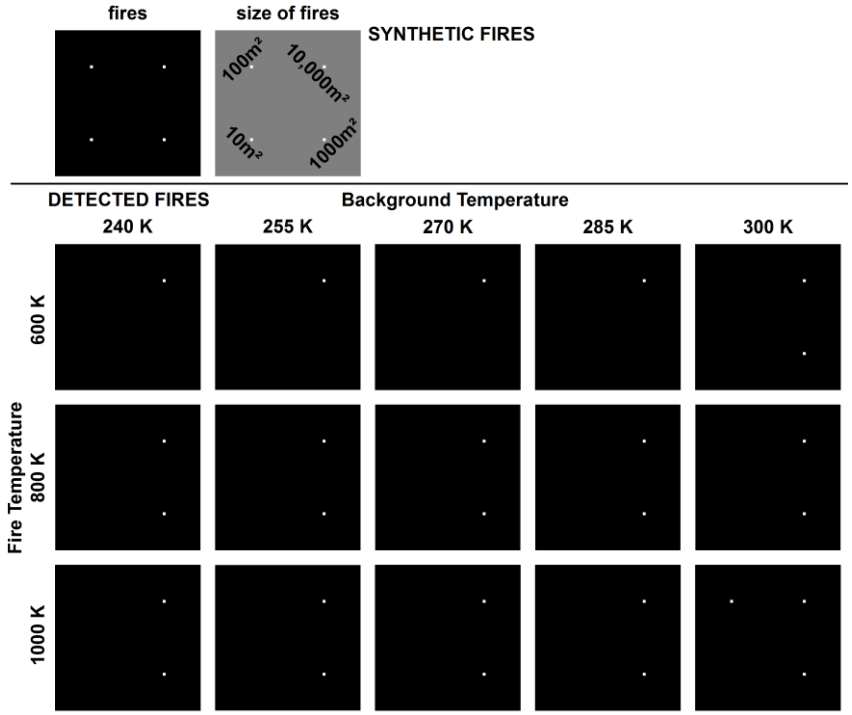

Figure 2. Results of the fire detection for the simulated dataset. The first row shows the simulated fires and their sizes. The second to forth rows show the detected fires by the hotspot algorithm. Different fire temperatures and background temperatures were tested. The background temperature is the same value all over the background and within the remaining area of the fire pixel not covered by the fire.

3.2. Validation with Real AVHRR Imagery

This section describes the validation of the results of the hotspot algorithm by using real AVHRR imagery. Five different datasets were used for the validation. The validation data were corrected for the cloud coverage of the AVHRR scene tested.

3.2.1. Results for Using MODIS Hotspot Data as Reference—Comparison with Original Algorithm

The developed procedure was validated with MODIS fire hotspots [83]. The MODIS sensor is installed on two platforms Terra and Aqua. Each covers the Earth twice a day. The validation of the hotspot detection was performed by using the hotspots derived from the MODIS acquisition with the shortest time difference to the AVHRR acquisition tested. For all three test sites mentioned below, data from the Aqua platform best fulfilled this requirement. Furthermore, to show the improvement of the

newly developed hotspot detection procedure in comparison to the original algorithm proposed by Giglio et al. [61], the same datasets were also processed with this original algorithm and validated against the same MODIS datasets. The validation described above was performed for three areas, Greece (August 2007), Sicily (July/August 2012) and Portugal (July/August/September 2012 and 2013). Table 5 shows the results of the validation procedure for the Greece 2007 test site. The number of true positives gives the number of AVHRR hotspots which match with the MODIS hotspots. False positives represent the number of overestimation (error of commission) of the AVHRR based hotspot algorithms in comparison with the MODIS reference data. False negatives show the number of MODIS fires not detected by AVHRR (error of omission). The true negatives represent the pixels which were not detected as fire at both AVHRR and MODIS. However, as the number of fires in a remote sensing scene such as AVHRR or MODIS is much lower than the number of pixels where no fire is detected, this last number is not presented here. The number of true negatives is not important for this analysis. Important is the number of correctly and missed fire detection as well as the number of fire overestimation (see above).

Comparison of the newly developed algorithm with the original one of Giglio et al. [61] shows that the number of true positives is slightly higher for the original algorithm. However, the number of false positives is with 95 much higher for Giglio et al. [61] than for the new algorithm (7). Both algorithms show a high tendency to miss MODIS fires. The number of false negatives is slightly higher for the new algorithm. Fires are short living phenomena. Some fires burn only a few minutes. The longer the time difference between the AVHRR acquisition and the MODIS acquisition used for reference, the higher is the possibility that the conditions on the ground changed. Therefore, the last row of Table 5 takes only those datasets into account, for which the time difference between the AVHRR and the MODIS acquisition is <30 min.

The results of the Sicily 2012 and the Portugal 2012/2013 test sites are shown in Tables 6 and 7. The values for the true positives and the false negatives are very similar for both fire detection algorithms. However, the new algorithm clearly shows a lower number of false positives, i.e., the overestimation is much lower with the new algorithm.

The average value per scene over all test sites is for the new algorithm 5.0 true positives, 5.6 false positives, and 6.4 false negatives. For the algorithm proposed by Giglio et al. [61], the values are 5.2 for the true positives, 18.9 for the false positives and 6.3 for the false negatives. The values for the true positives and false negatives are very similar for both procedures. However, for Giglio et al. [61], the overestimation (i.e., the number of false positives) is more than three times higher than for the new algorithm.

Table 5. Results of the validation for the Greece 2007 test site. Reference: MODIS (Aqua) hotspots.

Date	NOAA Satellite/AVHRR Sensor	AVHRR Time (UTC)	MODIS Time (UTC)	Time Difference (min)	Proposed New Algorithm			Algorithm of Giglio et al. [61]		
					True Positives	False Positives	False Negatives	True Positives	False Positives	False Negatives
24 August 2007	18/3	11:20	11:25	5	1	2	11	2	16	10
24 August 2007	17/3	19:49	20:50	61	1	2	8	2	5	7
25 August 2007	18/3	11:10	12:08	58	2	1	17	3	20	16
25 August 2007	17/3	21:05	19:55	70	11	0	4	12	3	3
26 August 2007	18/3	11:00	11:12	12	2	1	21	4	19	19
30 August 2007	18/3	11:58	12:26	28	2	1	1	2	32	0
Sum all					**19**	**7**	**62**	**25**	**95**	**55**
Sum for time difference <30 min					**5**	**5**	**20**	**8**	**67**	**29**

Table 6. Results of the validation for the Sicily 2012 test site. Reference: MODIS (Aqua) hotspots.

Date	NOAA Satellite/AVHRR Sensor	AVHRR Time (UTC)	MODIS Time (UTC)	Time Difference (min)	Proposed New Algorithm			Algorithm of Giglio et al. [61]		
					True Positives	False Positives	False Negatives	True Positives	False Positives	False Negatives
9 June 2012	19/3	11:49	11:32	17	2	14	0	2	16	0
15 July 2012	19/3	12:09	12:45	36	6	18	9	4	26	11
16 July 2012	19/3	11:58	11:50	8	6	12	5	6	24	5
8 August 2012	19/3	11:15	11:56	41	9	2	11	9	5	11
8 August 2012	19/3	12:56	11:56	60	9	2	11	9	12	11
9 August 2012	19/3	11:05	12:39	94	2	4	8	2	13	8
9 August 2012	19/3	12:45	12:39	6	6	7	5	6	9	5
10 August 2012	19/3	12:34	11:44	50	6	6	1	6	10	1
Sum all					**46**	**65**	**50**	**44**	**115**	**52**
Sum for time difference <30 min					**14**	**33**	**10**	**14**	**49**	**10**

Table 7. Results of the validation for the Portugal 2012/2013 test site. Reference: MODIS (Aqua) hotspots.

Date	NOAA Satellite/AVHRR Sensor	AVHRR Time (UTC)	MODIS Time (UTC)	Time Difference (min)	Proposed New Algorithm			Algorithm of Giglio et al. [61]		
					True Positives	False Positives	False Negatives	True Positives	False Positives	False Negatives
2 September 2012	19/3	13:27	13:30	3	5	0	4	5	5	4
30 June 2013	19/3	13:17	13:00	17	1	13	1	1	29	1
22 July 2013	19/3	14:20	14:00	20	1	1	0	1	4	0
23 July 2013	19/3	14:18	13:05	73	1	6	0	1	7	0
11 August 2013	19/3	14:05	13:36	29	0	3	8	0	6	8
19 August 2013	19/3	14:19	14:25	6	3	2	3	3	7	3
22 August 2013	19/3	13:47	13:18	29	11	13	1	8	35	4
26 August 2013	19/3	13:05	14:31	86	1	1	7	1	25	7
31 August 2013	19/3	13:50	13:11	39	6	8	3	7	32	2
2 September 2013	19/3	13:29	12:59	30	2	4	8	2	33	8
4 September 2012	19/3	13:06	12:47	19	0	1	3	0	20	14
5 July 2013	19/3	14:02	13:18	44	0	4	1	0	8	1
12 August 2013	19/3	13:54	14:19	25	4	5	3	4	9	3
13 August 2013	19/3	13:43	13:24	19	5	14	1	5	35	1
15 August 2013	19/3	13:22	13:11	11	2	13	4	2	24	4
19 August 2013	19/3	12:04	12:48	44	8	0	1	8	9	1
20 August 2013	19/3	14:08	13:30	38	7	3	3	7	9	3
21 August 2013	19/3	13:57	14:12	15	7	10	13	7	21	13
23 August 2013	19/3	13:36	14:00	24	2	4	5	2	30	5
24 August 2013	19/3	13:25	13:05	20	7	4	5	8	13	4
25 August 2013	19/3	13:15	13:48	33	7	2	17	7	34	17
28 August 2013	19/3	14:22	14:19	3	4	7	5	5	19	4
29 August 2013	19/3	12:32	13:24	52	1	0	19	4	6	14
29 August 2013	19/3	14:11	13:24	47	16	5	4	17	21	3
30 August 2013	19/3	14:00	14:06	6	16	14	2	16	42	2
1 September 2013	19/3	13:39	13:54	15	8	3	9	9	26	8
Sum all					**125**	**140**	**130**	**130**	**509**	**134**
Sum for time difference <30 min					**76**	**107**	**67**	**76**	**325**	**78**

3.2.2. Results for Using Visually Confirmed MODIS Hotspot Data as Reference

Next, an additional validation was performed by using only those MODIS fire hotspots for which the fire activity could be confirmed by analysis of the visible MODIS bands. Visible smoke was used as an indicator for fire activity. This analysis was performed by means of the NASA WorldView [84]. The aforementioned MODIS hotspot reference dataset, which was used in Section 3.2.1 [83], was used in addition to guarantee that a MODIS hotspot visible in the NASA WorldView is also represented in the database used in the previous validation. The problem with NASA WorldView is that it shows all MODIS hotspots of a certain day, acquired by Terra or Aqua. However, we are only interested in the MODIS hotspots which were acquired at a certain time (i.e., at the ascending or descending pass of Terra or Aqua). Therefore, the dataset described in Section 3.2.1 was used for filtering the NASA WorldView dataset.

Fire hotspots with a smoke plume visible at the spatial resolution of MODIS (250 m) usually represent larger fire events. Thus, this validation procedure tests whether the AVHRR-based processor is able to detect these larger fires. As shown in Section 3.2.1, the number of true positives and false negatives is more or less the same for the new developed approach and the algorithm proposed by Giglio et al. [61]. The benefit of the new algorithm is its smaller overestimation (number of false positives). However, the current validation procedure described in this section does not investigate the overestimation. Therefore, this validation approach was only performed for the results of the newly developed procedure.

As NASA WorldView does not contain MODIS data older than May 2012, this validation was only performed for the test sites Sicily (2012) and Portugal (2012/2013) and not for the Greece 2007 test site. Table 8 shows the results of this second validation procedure for the Sicily 2012 test site. Sixty-seven percent of the reference data were detected by AVHRR hotspots.

Table 8. Results of the validation for the Sicily 2012 test site. Reference: confirmed MODIS (Aqua) hotspots. The AVHRR satellite and sensor is described in Table 6.

Date	AVHRR Time (UTC)	MODIS Time (UTC)	Time Difference (min)	#Confirmed MODIS Hotspots	Reference Hotspots Detected by AVHRR
15 July 2012	12:09	12:45	36	7	57%
16 July 2012	11:58	11:50	8	6	17%
8 August 2012	11:15	11:56	41	4	100%
8 August 2012	12:56	11:56	60	4	100%
9 August 2012	11:05	12:39	94	1	0%
9 August 2012	12:45	12:39	6	1	100%
10 August 2012	12:34	11:44	50	4	100%
Sum or overall percentage				**27**	**67%**

For the Portugal 2012/2013 test site 51% of the visually confirmed MODIS hotspots were detected by AVHRR (Table 9).

Table 9. Results of the validation for the Portugal 2012/2013 test site. Reference: confirmed MODIS (Aqua) hotspots. The AVHRR satellite and sensor is described in Table 7.

Date	AVHRR Time (UTC)	MODIS Time (UTC)	Time Difference (min)	#Confirmed MODIS Hotspots	Reference Hotspots Detected by AVHRR
2 September 2012	13:27	13:30	3	4	50%
30 June 2013	13:17	13:00	17	1	0%
22 July 2013	14:20	14:00	20	1	100%
23 July 2013	14:18	13:05	73	1	100%
11 August 2013	14:05	13:36	29	8	0%
19 August 2013	14:19	14:25	6	3	67%
22 August 2013	13:47	13:18	29	10	80%

Table 9. *Cont.*

Date	AVHRR Time (UTC)	MODIS Time (UTC)	Time Difference (min)	#Confirmed MODIS Hotspots	Reference Hotspots Detected by AVHRR
26 August 2013	13:05	14:31	86	8	13%
31 August 2013	13:50	13:11	39	6	67%
2 September 2013	13:29	12:59	30	9	22%
4 September 2012	13:06	12:47	19	0	0%
5 July 2013	14:02	13:18	44	1	0%
12 August 2013	13:54	14:19	25	6	67%
13 August 2013	13:43	13:24	19	2	100%
15 August 2013	13:22	13:11	11	3	33%
19 August 2013	12:04	12:48	44	6	83%
20 August 2013	14:08	13:30	38	2	50%
21 August 2013	13:57	14:12	15	4	50%
23 August 2013	13:36	14:00	24	3	33%
24 August 2013	13:25	13:05	20	5	60%
25 August 2013	13:15	13:48	33	6	50%
28 August 2013	14:22	14:19	3	4	50%
29 August 2013	12:32	13:24	52	4	25%
29 August 2013	14:11	13:24	47	4	100%
30 August 2013	14:00	14:06	6	5	80%
1 September 2013	13:39	13:54	15	4	50%
	Sum or overall percentage			**110**	**51%**

The average detection rate at the two aforementioned test sites Sicily 2012 and Portugal 2012/2013 is for the second validation procedure 54%. When taking only those datasets where the time difference between the AVHRR and the MODIS acquisition is less than 10 min into account, the average detection rate increases to 58%.

3.2.3. Results for Using EFFIS Fire-News Data as Reference

A third test was applied to the Sicily and Portugal dataset: "real" fires reported by the European Forest Fire Information System (EFFIS) fire-news [85] were used as validation dataset. The sources of the EFFIS fire-news database are newspaper articles and media reports. Information about the location of the fire, the size of burnt area, the start and end date (but not the exact time) of the fire event, whether the fire is critical for the local people are provided. However, the information content varies strongly from event to event. As, of course, not every fire that occurs is included in the EFFIS fire-news, the validation could only test whether the AVHRR hotspot processor is able to detect these "real" EFFIS fires. Again, the results of the newly developed hotspot processor were tested. Table 10 shows the results of the third validation procedure for the Sicily 2012 test site. Fifty-three percent of the reference data were detected by AVHRR hotspots, while 47% were missed.

Table 10. Results of the validation for the Sicily 2012 test site. Reference: EFFIS fire-news.

Date	AVHRR Time (UTC)	#EFFIS Fire-News Fires	Reference Hotspots Detected by AVHRR
15 July 2012	12:09	3	33%
16 July 2012	11:58	5	80%
8 August 2012	11:15	9	44%
8 August 2012	12:56	9	44%
9 August 2012	11:05	3	100%
9 August 2012	12:45	3	33%
	Sum or overall percentage	**32**	**53%**

At the Portugal 2012/2013 test site 26% of the EFFIS fire-news fires were detected by AVHRR (Table 11).

The average detection rate at the two aforementioned test sites Sicily 2012 and Portugal 2012/2013 is for the third validation procedure 35%.

Table 11. Results of the validation for the Portugal 2012/2013 test site. Reference: EFFIS fire-news.

Date	AVHRR Time (UTC)	#EFFIS Fire-News Fires	Reference Hotspots Detected by AVHRR
2 September 2012	13:27	5	20%
30 June 2013	13:17	4	25%
23 July 2013	14:18	2	50%
11 August 2013	14:05	1	0%
19 August 2013	14:19	2	0%
22 August 2013	13:47	10	30%
26 August 2013	13:05	2	50%
2 September 2013	13:29	6	17%
4 September 2012	13:06	7	0%
12 August 2013	13:54	4	50%
13 August 2013	13:43	1	0%
21 August 2013	13:57	2	50%
23 August 2013	13:36	8	25%
24 August 2013	13:25	1	0%
25 August 2013	13:15	1	0%
28 August 2013	14:22	4	25%
29 August 2013	12:32	2	50%
29 August 2013	14:11	2	50%
Sum or overall percentage		**66**	**26%**

3.2.4. Results for Using Copernicus Emergency Management Service Data as Reference

The burnt area mapping products of the Copernicus Emergency Management Service (EMS) [86] are a valuable information source for validating the results of hotspot detection algorithms. The EMS generally uses data of very high spatial resolution pre and post-event optical satellite data to map the burnt area during or in the most cases after a fire event. In this article, the burnt area mapped by the EMS after the fire was used to test whether a hotspot within the EMS burnt area could be detected in an AVHRR scene, which was acquired during the fire event.

For the aforementioned test sites no EMS activation exists. Therefore, a fourth test sites was analyzed. The test was performed at a site in Sweden where a fire occurred in beginning of August 2014. The burnt area mapping by EMS shown in Figure 3 was used for validation (Table 12). The test with five AVHRR scenes showing no cloud coverage over the area of interest (AoI) results in a detection rate of 40%.

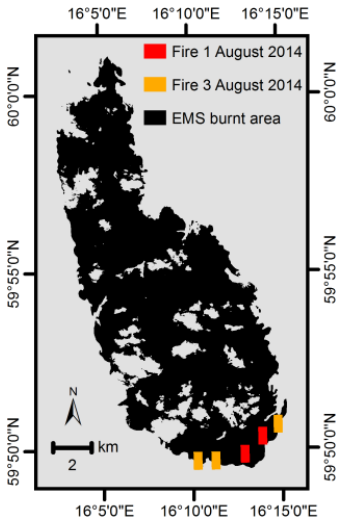

Figure 3. Test site Sweden 2014. Red and orange pixels show the detected AVHRR fire hotspots on 1 and 3 August 2014, respectively. Copernicus EMS burnt area mapping (black) is used as reference.

Table 12. Results of the validation for the Sweden 2014 test site. Reference: Copernicus EMS.

Date	AVHRR Time (UTC)	#Copernicus EMS Fires	Reference Hotspots Detected by AVHRR
01 August 2014	01:46	1	100%
02 August 2014	03:16	1	0%
03 August 2014	01:24	1	100%
03 August 2014	03:05	1	0%
03 August 2014	11:14	1	0%
	Sum or overall percentage	**5**	**40%**

3.2.5. Results for Using the Fire Database of Piedmont as Reference

Finally, to also test data of the AVHRR sensor generation 2, an event of forest fires that occurred on 5 February 1999 in Piedmont (northwest Italy) was analyzed by AVHRR imagery. The first MODIS sensor was launched in December 1999. Thus, no MODIS hotspots are available for this event. The Piedmont fire database [87] provides information about the communities which reported fires in their neighborhood, the date of the fire event and the size of the burnt area. According to this database, the surroundings of three local communities, Sala Biellese, Chiaverano and Courgnè, were affected by forest fires. Figure 4 shows that the AVHRR fires detected by the proposed hotspot processor are located in the close neighborhood to the communities which reported on 5 February 1999 for their surroundings strong destruction due to forest fires.

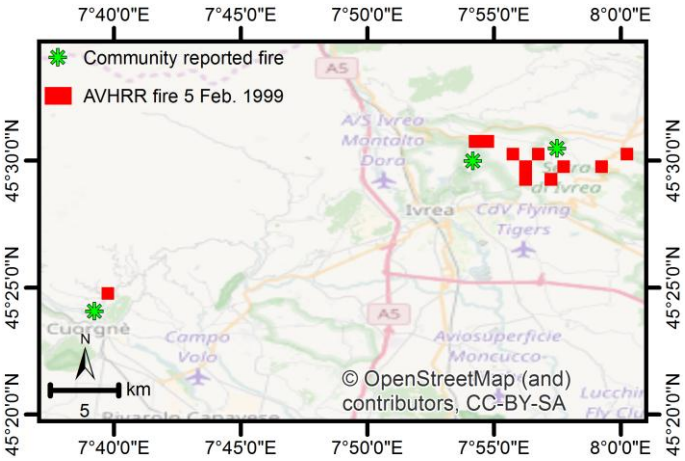

Figure 4. Forest fires in Piedmont, northwest Italy, on 5 February 1999. The fire hotspots detected by the proposed AVHRR imagery based processor (red) are in close neighborhood to the local communities which reported forest fires in the surroundings (green). Background: OpenStreetMap.

4. Discussion

This article presents an enhanced version of the hotspot detection processor proposed by Giglio et al. [61]. The developed hotspot detection processor is designed for an automatic processing of a long time-series of AVHRR data of a large AoI (cf. Section 2).

Suitable reference data of fire events are very rare. "Suitable" means that there occurred a fire event exactly at the date and time of an AVHRR overpass at cloud-free conditions and that we know the exact location of the fire, its size, temperature, beginning and ending of the event. As such, accurate reference data is not available, a first test of the proposed hotspot detection processor was performed with simulated fire data. As described in Section 3.1, 60 different conditions were tested, including different sizes of the fire (10 m^2, 100 m^2, 1000 m^2, and 10,000 m^2), different fire temperatures (600 K, 800 K, and 1000 K) and different background temperatures for the remaining area of the fire pixel, which is not covered by the fire, and for the pixels surrounding the fire pixel (245 K, 255 K, 270 K,

285 K, and 300 K). The simulation was performed under simplified conditions, i.e., only the brightness temperature values of T_3 were changed (while the difference of T_3 and T_4 was kept stable) and the area surrounding the fire pixel was assumed to have homogenous background temperature. In reality, a heterogeneous background and a variable value of T_4 makes the detection of fire events somehow more complicated [88]. Nevertheless, the simulation under simplified conditions clearly showed that the proposed hotspot detection algorithm is only able to detect "cooler" fires (~600 K), if these have an area ≥10,000 m^2. Hotter fires (≥800 K) are detected even at a smaller size of ≥1000 m^2. Very hot fires (>1000 K) are detected at even smaller sizes of ca. 100 m^2. This is in accordance with the original processor of Giglio et al. [61].

An important influencing factor on the detection of hotspots is the temperature thresholds of the fire candidates (Table 2). If these thresholds would be lower, the procedure could also detect smaller fires with a lower resulting average temperature of the fire pixel. However, lower thresholds for the selection of the candidates would result in a strong overestimation of fires, especially in areas of a warmer background >300 K, i.e., small parts of urban area and bare lands which are missed by the exclusion masks (Section 2.2.1) and which are characterized by warm temperatures in summer.

To test the practical usability of the proposed AVHRR data-based hotspot processor, it was tested under real conditions with a series of real AVHRR imagery (see Section 3.2). Five different validation procedures were performed.

The first validation used MODIS hotspots (MOD14A1) as a reference. We used MODIS hotspots derived from MODIS data acquired with the shortest temporal difference to the AVHRR scene tested. The Tables 5–7 show a relatively high number of false negatives, i.e., MODIS hotspots not detected by the AVHRR based algorithm. This can be explained by the circumstance that the AVHRR based processor misses especially smaller fires (cf. simulation, Section 3.1). Another reason for the relatively high number of false positives and false negatives could be the time difference between the MODIS acquisition and the AVHRR scene. Fires are short living phenomena (minutes to hours). Tables 5–7 also show the results only for AVHRR scenes where the reference MODIS scene was acquired at a time difference of less than 30 min. However, the relationship between the true positives and the false alarms is more or less stable compared to the result for all AVHRR scenes. The relatively high number of false alarms could be explained by the reason that overall MODIS is better suited for fire detection than AVHRR. One example is the very low saturation temperature of the AVHRR channel 3 (322 to 331 K). The corresponding channel of MODIS saturates at ca. 500 K [89], i.e., the thresholds for selecting the fire candidates can be set higher for MODIS, enabling a detection of fires at areas of warmer backgrounds. Moreover, MODIS is able to detect hotter and larger fires where the AVHRR channels already saturate.

To show the improvements of the new developed procedure, also the original algorithm of Giglio et al. [61], which serves as basis for the new algorithm, was implemented and the same AVHRR datasets where processed and validated with the same MODIS reference datasets. Comparison of the original and the new developed algorithm shows that the number of true positives (5.2 and 5.0 as an average of all validated AVHRR scenes) and the number of false negatives (6.3 and 6.4) are very similar for both algorithms. The great improvement of the new algorithm is the strong reduction of the number of false positives. The number of overestimated AVHRR fires is more than three times lower with the new algorithm compared to the original one of Gigilo et al. [61] (cf. Section 3.2.1). The reason for this is the more conservative approach of the new algorithm. The use of the LULC and especially the use of the GUF for exclusion of bare land areas and urban areas strongly help to reduce the number of false positives. Furthermore, the new algorithm searches only for fires at areas with certain vegetation cover, i.e., for areas, which are characterized by enough fuel for a wild fire. This is realized by the use of the FVC to exclude areas of only sparse vegetation.

The use of the FVC, the GUF and the LULC for exclusion of non-vegetated areas seems on the first look duplication. The reasons for the use of these three layers are as follows: The LULC serves as basis for exclusion of water areas and land areas free of vegetation. The GUF has a much higher

spatial resolution and is used to improve the exclusion of especially smaller urban areas, which are not included in the LULC. As the geolocation of the pre-processed L1b AVHRR imagery is not always completely accurate (geolocation differences of several kilometers have been observed at some AVHRR scenes), the FVC, which is directly computed from the AVHRR scene, is used to exclude areas free of vegetation, for such cases where there is a discrepancy of the location of the LULC/GUF and the AVHRR scene.

With both sensors, AVHRR and MODIS, one is not able to detect all fires on ground. Several studies showed that especially the error of omission is relatively high e.g., [82,90]. Especially smaller and "cooler" fires are not detected (cf. Section 3.1). Moreover, as confirmed by, e.g., Cardoso et al. [91], MODIS active fires are characterized by a high commission error. To test the proposed AVHRR hotspot detection processor for "real" occurred fires, a second validation was performed using only those MODIS fire hotspots for which the fire activity could be confirmed by visual analysis of the visual bands, i.e., only MODIS hotspots were used where a smoke was visible. Of course, this means that we will not consider smaller fires, where the smoke plume is too small to be visible at the spatial resolution of MODIS. However, this second validation ensures that we test the AVHRR hotspot processor for hotspots where MODIS did not overestimate the fire activity. This test allowed only to test whether the new developed AVHRR-based processor is able to detect these visually confirmed MODIS hotspots. Overestimation of the AVHRR procedure could not be validated as in Section 3.2.1. On average, ca. 54% of the visually confirmed MODIS hotspots could be detected by the proposed algorithm. When considering only those datasets, where the time difference between the AVHRR and the MODIS acquisition is less than 10 min, the average detection rate increases to 58%.

A third test with in-situ confirmed fires was applied (cf. Section 3.2.3). EFFIS fire-news reports were used for the validation. The average detection rate of these EFFIS fire-news fires is with 35% very low. As mentioned in Section 3.2.3, the sources of the EFFIS fire-news database are newspaper articles and media reports. The information content varies strongly from event to event. In most cases, no information is provided about the size of the burnt area. Moreover, only the date of the fire event is provided, but no information about the exact time of the fire event (start and end time). Therefore, due to the short living times of fires (minutes to hours) there is a high probability that a certain fire was not active at the time for the AVHRR overfly. In addition, the information about the location of the fire is not always very accurate, i.e., as location often the town next to the fire event is provided. Nevertheless, we used the EFFIS fire-news dataset for an additional validation, as this dataset provides information of fires confirmed on the ground. Due to the missing time information the EFFIS fire-news dataset is not an ideal dataset for validation.

The fourth validation procedure based on a burnt area mapping of the EMS as reference data resulted in a detection rate of 40%. In two of five AVHRR scenes, the fire was detected. The result of the EMS mapping is the final burnt area, after the fire event. The aim of the validation was to test whether the proposed AVHRR hotspot detection is able to detect during the time of the fire event an active fire within the EMS burnt area. As only AVHRR imagery showing no cloud coverage over the AoI was analyzed, cloud cover is no reason for the missing of the hotspot at three AVHRR scenes. The strength of a fire is very dynamic. At the last two acquisitions there was also no fire detected by AVHRR. According to the EMS mapping, the fire in Sweden lasted until 4 August 2014. However, the strength of the fire might have decreased near towards its end and the fire might be too small to be detected at these two last acquisitions.

Section 3.2.5 showed that the proposed fire hotspot processor also works well with "older" AVHRR imagery of sensor generation 2. The detected fires are in good agreement with reports of the Piedmont fire database [87]. As for the aforementioned validation by means of the EMS burnt area, for the validation procedure described in Section 3.2.5, it was only able to test whether the AVHRR processor detects fire hotspots within the area that is reported to have burnt at a certain date. For the last three validation procedures (Sections 3.2.3–3.2.5) only the dates of the fire events is known, not the exact time.

In the future, the described L2 hotspot product (cf. Section 1.4) will be enhanced to a L3 product, which will be based on the work of e.g., Pozo et al. [57] and Fraser et al. [92], i.e., a multi-temporal analysis of the AVHRR imagery will be implemented to increase the accuracy of the active fire mapping.

5. Conclusions

This paper presented a fully automated fire hotspot detection processor for the analysis of Advanced Very High Resolution Radiometer (AVHRR) data over the European continent. Three different probability levels of fire detection are provided. The presented algorithm is suited for day and night acquisitions.

A validation with simulated data under simplified conditions showed that the proposed algorithm is only able to detect "cooler" fires (~600 K), if these have an area $\geq$10,000 m^2. Hotter fires (>800 K) are detected even at a smaller size of $\geq$1000 m^2. Very hot fires (>1000 K) are detected at even smaller sizes of ca. 100 m^2.

The proposed processor is an enhanced version of the hotspot detection algorithm described by Giglio et al. [61]. The improvements of the new developed processor were demonstrated by processing the same AVHRR datasets with both, the original algorithm and the new developed one. The validation of both results was performed with the same reference data, with MODIS hotspots, derived from MODIS acquisitions with the shortest temporal difference to the AVHRR imagery tested. The great improvement of the new algorithm compared with the original one is the strong reduction of the number of false positives by more than three times, while keeping the number of true positives stable. The number of false negatives is very similar for both algorithms. The use of land cover and land use information, the incorporation of the global urban footprint and the consideration of a certain volume of vegetation required as fuel for fire events (derived by means of the fraction of vegetation computation), strongly help to reduce the number of false positives.

The hotspot processor is part of the German Aerospace Center's (DLR) TIMELINE project, which aims to develop an operational processing and data management environment to process 30 years of NOAA-AVHRR raw data into L1b, L2 and L3 products. The paper presented the current status of the L2 hotspot processor, which is based on single-temporal datasets in orbit geometry. It is planned to further enhance this processor, including multi-temporal analysis to produce more reliable data on fire hotspots. These steps are part of the planned L3 hotspot product.

Furthermore, as described in Section 2, within the TIMELINE project, enhanced algorithms for cloud and water detection have been developed [93,94]. These enhanced cloud and water masks will replace the currently used simplified algorithms for cloud and water detection described in Section 3.1. Enhanced exclusion masks will further improve the quality of the TIMELINE hotspot detection processor.

Acknowledgments: The authors thank the entire TIMELINE team for fruitful cooperation and discussion. This work has been funded by DLR. The authors would like to thank the anonymous reviewers for their very constructive remarks.

Author Contributions: Eva-Maria Fuchs wrote the introduction and developed the first steps of the hotspot processor. Simon Plank, the principle author, wrote the main part of the paper, developed further the hotspot processor and performed the validation. Corinne Frey supported the development and provided suggestions for its improvement. All authors read, revised and approved the final manuscript.

Conflicts of Interest: The authors declare no conflict of interest.

References

1. Viegas, D.; Ribeiro, L.; Viegas, M.; Pita, L.; Rossa, C. Impacts on fire on society: Extreme fire propagation issues. In *Earth Observation of Wildland Fires in Mediterranean Ecosystems*; Chuvieco, E., Ed.; Springer: Berlin/Heidelberg, Germany, 2009; pp. 97–408.
2. Margaris, N.; Koutsidou, E.; Giourga, C. Changes in traditional Mediterranean land-use systems. In *Mediterranean Desertification and Land Use*; Brandt, C., Thornes, J., Eds.; Wiley: New York, NY, USA, 1996.

3. Médail, F. Mediterranean. In *Ecosystem Ecology*; Jorgensen, S.E., Ed.; Elsevier: Amsterdam, The Netherlands, 2016; pp. 319–330.
4. Beringer, J.; Hutley, L.B.; Tapper, N.J.; Coutts, A.; Kerley, A.; Grandy, A.P. Fire impacts on surface heat, moisture and carbon fluxes from a tropical savanna in northern Australia. *Int. J. Wildl. Fire* **2003**, *12*, 333–340. [CrossRef]
5. Chuvieco, E. Earth Observation of Global Change. In *The Role of Satellite Remote Sensing in Monitoring the Global Environment*; Springer: Berlin/Heidelberg, Germany, 2008.
6. Wotawa, G.; Novelli, P.C.; Trainer, M.; Granier, C. Inter-annual variability of summertime CO concentrations in the Northern Hemisphere explained by boreal forest fires in North America and Russia. *Geophys. Res. Lett.* **2001**, *28*, 4575–4578. [CrossRef]
7. Crutzen, P.J.; Heidt, L.E.; Krasnec, J.P.; Pollock, W.H.; Seiler, W. Biomass burning as a source of atmospheric gases CO, H_2, N_2O, NO, CH_2CI, and COS. *Nature* **1979**, *282*, 253–256. [CrossRef]
8. Crutzen, P.J.; Graedel, T.E. The Role of atmospheric chemistry in environment-development interactions. In *Sustainable Development of the Biosphere*; Clark, W.C., Munn, R.E., Eds.; Cambridge University Press: Cambridge, UK, 1987; pp. 213–249.
9. Crutzen, P.J.; Andreae, M.O. Biomass burning in the tropics: Impact on atmospheric chemistry and biogeochemical cycles. *Science* **1990**, *250*, 1669–1678. [CrossRef] [PubMed]
10. Setzer, A.; Pereira, M. Amazonia biomass burnings in 1987 and an estimate of their tropospheric emissions. *Ambio* **1991**, *20*, 19–23.
11. Khazenie, N.; Richardson, K.A. Detection of oil fire smoke over water in the Persian Gulf Region. *Photogramm. Eng. Remote Sens.* **1993**, *59*, 1271–1276.
12. Levine, J.S.; Cofer, W.R.; Cahoon, D.R.; Winstead, E.L. Biomass burning: A driver for global change. *Environ. Sci. Technol.* **1995**, *29*, 120–125.
13. Weber, G.; Stocks, B. Forest fires and sustainability in the boreal forest of Canada. *Ambio* **1998**, *27*, 545–550.
14. Schulz, M.G.; Jacob, D.J.; Wang, Y.; Logan, J.A.; Atlas, E.L.; Blake, D.R.; Blake, N.J.; Bradshaw, J.D.; Browell, E.V.; Fenn, M.A.; et al. On the origin of tropospheric ozone and NO_x over the tropical South Pacific. *J. Geophys. Res.* **1999**, *104*, 5829–5843. [CrossRef]
15. Eva, H.; Lambin, E.F. Remote sensing of biomass burning in tropical regions: Sampling issue and multisensory approach. *Remote Sens. Environ.* **1998**, *64*, 292–315. [CrossRef]
16. Langaas, S.; Muirhead, K. Monitoring bushfires in West Africa by weather satellites. In Proceedings of the 22nd International Symposium on Remote Sensing of Environment, Abidjan, Ivory Coast, 20–26 October 1988.
17. Khattak, K.B.; Vaughn, R.A.; Cracknell, A.P. Sunglint and its observation in AVHRR data. *Remote Sens. Environ.* **1991**, *37*, 101–116. [CrossRef]
18. Goward, S.N.; Markham, B.; Dye, D.G.; Dulaney, W.; Yang, J. Normalized difference vegetation index measurements from the Advanced Very High Resolution Radiometer. *Remote Sens. Environ.* **1991**, *35*, 257–277. [CrossRef]
19. Privette, J.L.; Fowler, C.; Wick, G.A.; Baldwin, D.; Emery, W.J. Effects of orbital drift on advanced very high resolution radiomter products: Normalized difference vegetation index and sea surface temperature. *Remote Sens. Environ.* **1995**, *53*, 164–171. [CrossRef]
20. Robinson, J.M. Fire from space: Global fire evaluation using infrared remote sensing. *Int. J. Remote Sens.* **1991**, *12*, 3–24. [CrossRef]
21. Li, Z.; Cihlar, J.; Moreau, L.; Huang, F.; Lee, B. Monitoring fire activities in the boreal ecosystem. *J. Geophys. Res.* **1997**, *102*, 29611–29624. [CrossRef]
22. Casanova, J.L.; Illera, P.; Delgado, J.A.; Rodriguez, P. Analisis de incendios mediante imagenes NOAA. *Teledetección y medio ambiente. Junta de Andalucia* **1991**, *1991*, 40–45.
23. Dietz, A.; Bachmann, M.; Frey, C. Automated improvement of geolocation accuracy in AVHRR data using a twin-sided chipmatching approach—A TIMELINE thematic processor. *Remote Sens.* **2017**. under review.
24. Bachmann, M.; Tungalagsaikhan, P.; Ruppert, T.; Dech, S. Calibration and pre-processing of a multi-decadal AVHRR time series. In *Remote Sensing Time Series—Revealing Land Surfece Dynamics. Remote Sensing and Digital Image Processing*; Kuenzer, C., Dech, S., Wagner, W., Eds.; Springer: Heidelberg, Germany, 2015; pp. 43–74.

25. Bachmann, M.; Dietz, A.; Ruppert, T.; Müller, T.; Frey, C. TIMELINE—L1b-Preprocessor & CalVal. In Proceedings of the ESA Workshop—Long-Term Data Preservation (LTDP), Oberpfaffenhofen, Germany, 20–21 April 2015.
26. Kennedy, P.; Belward, A.; Grégoire, J.-M. An improved approach to fire monitoring in West Africa using AVHRR data. *Int. J. Remote Sens.* **1994**, *15*, 2235–2255. [CrossRef]
27. Malingreau, J.P. Remote sensing and disaster monitoring: A review of applications in Indonesia. In Proceedings of the 18th International Symposium on Remote Sensing of Environment, Paris, France, 1–5 October 1984; Environmental Research Institute of Michigan: Ann Arbor, MI, USA, 1985; Volume 1, pp. 283–297.
28. Malingreau, J.P.; Stpehens, G.; Fellows, L. Remote sensing of forest fires: Kalimantan and North Borneo in 1982–83. *Ambio* **1985**, *14*, 314–321.
29. Matson, M.; Holben, B. Satellite detection of tropical burning in Brazil. *Int. J. Remote Sens.* **1987**, *8*, 509–516. [CrossRef]
30. Kaufman, Y.J.; Tucker, C.J.; Fung, I. Remote sensing of biomass burning in the tropics. *J. Geophys. Res.* **1990**, *95*, 9895–9939. [CrossRef]
31. Prins, E.M.; Menzel, W.P. Geostationary satellite detection of bio mass burning in South America. *Int. J. Remote Sens.* **1992**, *13*, 2783–2799. [CrossRef]
32. Pereira, M.C.; Setzer, A.W. Spectral characteristics of deforestation fires in NOAA/AVHRR images. *Int. J. Remote Sens.* **1993**, *14*, 583–597. [CrossRef]
33. Eva, H.; Flasse, S. Contextual and multiple-threshold algorithms for regional active fire detection with AVHRR. *Remote Sens. Rev.* **1996**, *14*, 333–351. [CrossRef]
34. Justice, C.O.; Kendall, J.D.; Dowty, P.R.; Scholes, R.J. Satellite remote sensing of fires during the SAFARI campaign using NOAA advanced very high resolution radiometer data. *J. Geophys. Res.* **1996**, *101*, 823–851. [CrossRef]
35. Olson, J.R.; Baum, B.A.; Cahoon, D.R.; Crawford, J.H. Frequency and distribution of forest, savanna, and crop fires over tropical regions during PEM-Tropics A. *J. Geophys. Res.* **1999**, *104*, 5865–5876. [CrossRef]
36. Bowman, D.M.J.S.; Zahng, Y.; Walsh, A.; Williams, R.J. Experimental comparison of four remote sensing techniques to map tropical savanna fire-scars using Landsat-TM imagery. *Int. J. Wildl. Fire* **2003**, *12*, 341–348. [CrossRef]
37. Chung, Y.-S.; Le, H.V. Detection of fire smoke plumes by satellite imagery. *Atmos. Environ.* **1984**, *18*, 2143–2151. [CrossRef]
38. Flannigan, M.D.; Vonder Haar, T.H. Forest fire monitoring using NOAA satellite AVHRR. *Can. J. For. Res.* **1986**, *16*, 975–982. [CrossRef]
39. Cahoon, D.R.; Stocks, B.J.; Levine, J.S.; Cofre, W.R.; Pierson, J.M. Satellite analysis of the severe 1987 forest fires in Northern China and Southeastern Siberia. *J. Geophys. Res.* **1994**, *99*, 18627–18638. [CrossRef]
40. Li, Z.; Nadon, S.; Cihlar, J. Satellite-based detection of Canadian boreal forest fires: Development and application of the algorithm. *Int. J. Remote Sens.* **2000**, *21*, 3057–3069. [CrossRef]
41. Rauste, Y.; Herland, E.; Frelander, H.; Soni, K.; Kuoremaki, T.; Roukari, A. Satellite-based forest fire detection for fire control in boreal forests. *Int. J. Remote Sens.* **1997**, *18*, 2641–2656. [CrossRef]
42. Boles, H.S.; Verbyla, D.L. Comparison of Three AVHRR-Based Fire Detection Algorithms for Interior Alaska. *Remote Sens. Environ.* **2000**, *72*, 1–16. [CrossRef]
43. Soja, A.J.; Sukhinin, A.I.; Cahoon, D.R.; Shugart, H.H.; Stackhouse, P.W. AVHRR-derived fire frequency, distribution and area burned in Siberia. *Int. J. Remote Sens.* **2004**, *25*, 1939–1960. [CrossRef]
44. Kasischke, E.; French, N. Locating and estimating the area extent of wildfires in Alaskan Boreal forests using multiple-season AVHRR NDVI composite data. *Remote Sens. Environ.* **1995**, *51*, 263–275. [CrossRef]
45. Muirhead, K.; Cracknell, A.P. Straw burning over Great Britain detected by AVHRR. *Int. J. Remote Sens.* **1985**, *6*, 827–833. [CrossRef]
46. Djavadi, D.; Cracknell, A.P. Cloud cover and the monitoring of strawburning using AVHRR data. *Int. J. Remote Sens.* **1986**, *7*, 949–951. [CrossRef]
47. Saull, R.J. Strawburning over Great Britain detected by AVHRR: A comment. *Int. J. Remote Sens.* **1986**, *7*, 169–172. [CrossRef]
48. Cracknell, A.P.; Saradjian, M.R. Monitoring of straw burning in the U.K. using AVHRR data—Summer 1995. *Int. J. Remote Sens.* **1996**, *17*, 2463–2466. [CrossRef]

49. Langaas, S. Temporal and spatial distribution of savanna fires in Senegal and the Gambia, West Africa, 1989–1990, derived from multi-temporal AVHRR night images. *Int. J. Wildl. Fire* **1992**, *2*, 21–36. [CrossRef]
50. Langaas, S. A parametrised bispectral model for savanna fire detection using AVHRR night images. *Int. J. Remote Sens.* **1993**, *14*, 2245–2262. [CrossRef]
51. Pereira, A.C.; Setzer, A.W. Comparison of fire detection in savannas using AVHRR's channel 3 and TM images. *Int. J. Remote Sens.* **1996**, *17*, 1925–1937. [CrossRef]
52. Chuvieco, E.; Martin, M.P. A simple method for fire growth mapping using AVHRR channel 3 data. *Int. J. Remote Sens.* **1994**, *15*, 3141–3146. [CrossRef]
53. Illera, P.; Fernández, A.; Delgado, J.A. Fire monitoring in Spain using NOAA thermal data and NDVI. In *Sensors and Environmental Applications for Remote Sensing*; Asken, J., Ed.; Balkema: Rotterdam, The Netherlands, 1995; pp. 377–383.
54. Fernández, A.; Illera, P.; Casanova, J.L. Automatic mapping of surfaces affected by forest fires in Spain using AVHRR NDVI composite image data. *Remote Sens. Environ.* **1997**, *60*, 153–162. [CrossRef]
55. Dozier, J. A method for the satellite identification of surface temperature fields of subpixel resolution. *Remote Sens. Environ.* **1981**, *11*, 221–229. [CrossRef]
56. Dowty, P. The simulation of AVHRR data for the evaluation of fire-detection techniques. In *Biomass Burning and Global Change*; Levine, J.S., Ed.; MIT Press: Cambridge, MA, USA, 1996; pp. 25–39.
57. Pozo, D.; Olmo, F.J.; Alados-Arboledas, L. Fire detection and growth monitoring using a multitemporal technique on AVHRR mid-infrared and thermal channels. *Remote Sens. Environ.* **1997**, *60*, 111–120. [CrossRef]
58. Arino, O.; Melinotte, J.M. Cover the 1993 Africa Fire Map. *Int. J. Remote Sens.* **1998**, *19*, 2019–2023. [CrossRef]
59. Flasse, S.P.; Ceccato, P. A contextual algorithm for AVHRR fire detection. *Int. J. Remote Sens.* **1996**, *17*, 419–424. [CrossRef]
60. Harris, A.J. Towards automated fire monitoring from space: Semi-automated mapping of the January 1994 New South Wales wildfires using AVHRR data. *Int. J. Wildl. Fire* **1996**, *6*, 107–116. [CrossRef]
61. Giglio, L.; Kendall, J.D.; Justice, C.O. Evaluation of global fire detection algorithms using simulated AVHRR infrared data. *Int. J. Remote Sens.* **1999**, *20*, 1947–1985. [CrossRef]
62. Nakayama, M.; Elividge, C.D.; Liew, S.C. Contextual algorithm adapted for NOAA-AVHRR fire detection in Indonesia. *Int. J. Remote Sens.* **1999**, *20*, 3415–3421. [CrossRef]
63. Stroppiana, D.; Pinnock, S.; Gregoire, J.-M. The Global Fire Product: Daily fire occurrence from April 1992 to December 1993 derived from NOAA AVHRR data. *Int. J. Remote Sens.* **2000**, *21*, 1279–1288. [CrossRef]
64. Ressl, R.; Lopez, G.; Cruz, I.; Colditz, R.R.; Schmidt, M.; Ressl, S.; Jiménez, R. Operational active fire mapping and burnt area identification applicable to Mexican Nature Protection Areas using MODIS and NOAA-AVHRR direct readout data. *Remote Sens. Environ.* **2009**, *113*, 1113–1126. [CrossRef]
65. Kudoh, J.; Noguchi, S. A study of three-dimensional histogram using the NOAA AVHRR images. *IEEE Trans. Geosci. Remote Sens.* **1991**, *29*, 736–741. [CrossRef]
66. Cuomo, V.; Lasaponara, R.; Tramutoli, V. Evaluation of a new satellite-based method for forest fire detection. *Int. J. Remote Sens.* **2001**, *22*, 1799–1826. [CrossRef]
67. Pergola, N.; Marchese, F.; Tramutoli, V. Automated detection of thermal features of active volcanoes by means of infrared AVHRR records. *Remote Sens. Environ.* **2004**, *93*, 311–327. [CrossRef]
68. Kalpoma, K.A.; Kudoh, J.-I. A new algorithm for forest fire detection method with statistical analysis using NOAA AVHRR images. *Int. J. Remote Sens.* **2006**, *27*, 3867–3880. [CrossRef]
69. Lee, T.R.; Tag, P.M. Improved detection of hotspots using the AVHRR 3.7 μm channel. *Bull. Am. Meteorol. Soc.* **1990**, *71*, 1722–1730. [CrossRef]
70. Fuchs, E.; Stein, E.; Strunz, G.; Strobl, C.; Frey, C. Fire Monitoring—The use of medium resolution satellites (AVHRR, MODIS TET) for long time series processing and the implementation in user driven applications and services. In *The International Archives of the Photogrammetry, Remote Sensing and Spatial Information Sciences, Proceedings of the 36th International Symposium on Remote Sensing of Environment, Berlin, Germany, 11–15 May 2015*; International Society for Photogrammetry and Remote Sensing: Freiburg, Germany, 2015.
71. Cao, C.; Xiong, X.; Wu, A.; Wu, X. Assessing the Consistency of AVHRR and MODIS L1B Reflectance for Generating Fundamental Climate Data Records. *J. Geophys. Res. Atmos.* **2008**. [CrossRef]
72. Hao, X.; Qu, J.J. Development of the Global Multispectral Imager Thermal Emissive FCDRs. In *Satellite-Based Applications on Climate Change*; Qu, J., Powell, A., Sivakumar, M.V.K., Eds.; Springer: Dordrecht, The Netherlands, 2013; pp. 67–80.

73. Hansen, M.; DeFries, R.; Townshend, J.R.G.; Sohlberg, R. Global land cover classification at 1 km spatial resolution using a classification tree approach. *Int. J. Remote Sens.* **2000**, *21*, 1331–1365. [CrossRef]
74. Günther, K.P. *Cloud and Water Mask for L1B—AVHRR Data*, version 3; Internal Document; German Aerospace Center (DLR): Oberpfaffenhofen, Germany, 2015.
75. Giglio, L.; Kendall, J.D.; Mack, R. A multi-year active fire dataset for the tropics derived from the TRMM VIRS. *Int. J. Remote Sens.* **2003**, *20*, 4505–4525. [CrossRef]
76. Carlson, T.N.; Ripley, D.A. On the relation between NDVI, fractional vegetation cover, and leaf area Index. *Remote Sens. Environ.* **1997**, *62*, 241–252. [CrossRef]
77. Esch, T.; Taubenböck, H.; Roth, A.; Heldens, W.; Felbier, A.; Thiel, M.; Schmidt, M.; Müller, A.; Dech, S. TanDEM-X mission: New perspectives for the inventory and monitoring of global settlement patterns. *J. Sel. Top. Appl. Earth Obs. Remote Sens.* **2012**, *6*, 21. [CrossRef]
78. Lillesand, T.M.; Kiefer, R.W. *Remote Sensing and Image Interpretation*, 4th ed.; John Wiley & Sons: New York, NY, USA, 2000.
79. Gupta, R.P. *Remote Sensing Geology*; Springer: Heidelberg, Germany, 2003.
80. Albertz, J.; Wiggenhagen, M. *Guide for Photogrammetry and Remote Sensing*, 5th ed.; Wichmann: Paderborn, Germany, 2009.
81. Rouse, J.W.; Haas, R.H.; Schell, J.A.; Deering, D.W. Monitoring vegetation systems in the Great Plains with ERTS. In *Earth Resources Technology Satellite—1 Symposium*; 3rd, ed.; Volume I: Technical Presentations, NASA SP-351; NASA Goddard Space Flight Center: Greenbelt, MD, USA, 1973.
82. Morisette, J.; Giglio, L.; Csiszar, I.; Setzer, A.; Schroeder, W.; Morton, D.; Justice, C. Validation of MODIS active fire detection products derived from two algorithms. *Earth Interact.* **2004**, *9*, 1–25. [CrossRef]
83. NASA. Fire Information for Resource Management System (FIRMS). Available online: https://firms.modaps.eosdis.nasa.gov (accessed on 23 July 2016).
84. NASA WorldView. Available online: https://worldview.earthdata.nasa.gov/ (accessed on 25 July 2016).
85. European Forest Fire Information System (EFFIS). Available online: http://forest.jrc.ec.europa.eu/effis/applications/firenews/ (accessed on 22 July 2016).
86. Copernicus Emergency Management Service (EMS). Available online: http://emergency.copernicus.eu/mapping/ (accessed on 20 July 2016).
87. Banca Dati Incendi Boschivi, Sistemapiemonte. Forest Fire Database Piedmont. Available online: http://www.sistemapiemonte.it/incalfa/jsp/ricerca_inc/ricercaAvanzataInit.do (accessed on 20 September 2016).
88. Hawbaker, T.; Radeloff, V.; Syphard, A.; Zhu, Z.; Stewart, S. Detection rates of the MODIS active fire product in the United States. *Remote Sens. Environ.* **2008**, *112*, 2656–2664. [CrossRef]
89. Justice, C.; Giglio, L.; Boschetti, L.; Roy, D.; Csiszar, I.; Morisette, J.; Kaufman, Y. *Modis Fire Products*; Algorithm Technical Background Document; NASA Goddard Space Flight Center: Greenbelt, MD, USA, 2006.
90. Schroeder, W.; Prins, E.; Giglio, L.; Csiszar, I.; Schmidt, C.; Morisette, J.; Morton, D. Validation of GOES and MODIS active fire detection products using ASTER and ETM+ data. *Remote Sens. Environ.* **2008**, *112*, 2711–2726. [CrossRef]
91. Cardoso, M.F.; Hurtt, G.C.; Moore, B.; Nobre, C.A.; Bain, H. Field work and statistical analyses for enhanced interpretation of satellite fire data. *Remote Sens. Environ.* **2005**, *96*, 212–227. [CrossRef]
92. Frazer, R.H.; Li, Z.; Cihlar, J. Hotspot and NDVI Differencing Synergy (HANDS): A New Technique for Burned Area Mapping over Boreal Forest. *Remote Sens. Environ.* **2000**, *74*, 362–376. [CrossRef]
93. Dietz, A.; Frey, C. Detection of Water Bodies from AVHRR data applying a dynamic local threshold derived from near infrared reflectance—A TIMELINE thematic processor. *Remote Sens.* **2017**, under review.
94. Klüser, L.; Killius, N.; Gesell, G. APOLLO_NG—A probabilistic interpretation of the APOLLO legacy for AVHRR heritage channels. *Atmos. Meas. Technol.* **2015**, *8*, 4155–4170. [CrossRef]